Chinese Journal of
POLYMER SCIENCE

RESEARCH ARTICLE

https://doi.org/10.1007/s10118-026-3628-3
Chinese J. Polym. Sci. **2026**, *44*, 2144–2152

A Polymer Cathode Interlayer Based on B←N Unit for Suppressed Dark Current in Organic Photodetectors

Yu-Xin Xi[a,b], Ke Jia[a,b], Jia-Hui Wang[a,b], Xu Cao[a,b], Si-Hui Deng[a,b], Jun-Hui Miao[b], Xing-Xin Shao[b*], Jun Liu[a,b*], and Li-Xiang Wang[a,b]

[a] *School of Applied Chemistry and Engineering, University of Science and Technology of China, Hefei 230026, China*
[b] *State Key Laboratory of Polymer Science and Technology, Changchun Institute of Applied Chemistry, Chinese Academy of Sciences, Changchun 130022, China*

Electronic Supplementary Information

Abstract The development of high-performance cathode interlayers (CILs) with low-lying highest occupied molecular orbital (HOMO) energy levels (E_{HOMO}), capable of effectively suppressing dark current, is crucial for advancing organic photodetectors (OPDs). Herein, we report the first design of alcohol-soluble n-type conjugated polymers based on the boron-nitrogen coordination bond (B←N) unit, serving as CILs for high-performance OPDs. Benefiting from the strong electron-withdrawing capability of the B←N unit and the acceptor-acceptor (A-A) backbone, the polymer simultaneously achieves an E_{HOMO} of −5.88 eV and a high electrical conductivity of 1.36×10^{-6} S·cm^{-1}. An ultralow dark current density of 1.66×10^{-9} A·cm^{-2} under −1 V bias was achieved in OPDs incorporating this CIL, which is one order of magnitude lower than that of devices with the state-of-the-art CIL, resulting in a specific detectivity (D^*) of up to 1.86×10^{12} Jones in the near-infrared (NIR) region. To the best of our knowledge, this work represents the first report on B←N-unit-based n-type polymers as CILs for OPDs, providing a novel paradigm for designing next-generation ultra-low-noise optoelectronic devices.

Keywords B←N unit; Organic photodetectors; Dark current density; Low HOMO energy level

Citation: Xi, Y. X.; Jia, K.; Wang, J. H.; Cao, X.; Deng, S. H.; Miao, J. H.; Shao, X. X.; Liu, J.; Wang, L. X. A polymer cathode interlayer based on B←N unit for suppressed dark current in organic photodetectors. *Chinese J. Polym. Sci.* **2026**, *44*, 2144–2152.

INTRODUCTION

Near-infrared (NIR) photodetection has attracted extensive attention from both academic and industrial communities owing to its critical role in advanced technologies, including machine vision,[1,2] biomedical diagnostics,[3–5] and night vision systems.[6,7] Compared with conventional inorganic semiconductors and colloidal quantum dots, organic photodetectors (OPDs) have emerged as highly promising photodetection platforms owing to their solution processability, low fabrication cost, intrinsic mechanical flexibility, and absence of toxic heavy metals.[8–11] These advantages endow OPDs with great potential for portable and consumer-oriented optoelectronic applications.[12] Despite these advantages, the realization of high-sensitivity NIR OPDs, particularly under low-light conditions, remains fundamentally limited by excessive dark current.[13,14] In photodiode-type OPDs, undesired reverse hole injection from the cathode into the photoactive layer is a key factor in determining the dark current,[5] as it severely degrades the signal-to-noise ratio and constrains further improvements in specific detectivity. Consequently, the cathode interlayer (CIL) plays a pivotal role in governing device performance.[15–18] An ideal CIL must not only enable efficient electron extraction and transport, but also establish a robust energetic barrier that effectively suppresses hole back-injection at the cathode and active-layer interface.

Traditional cathode modification strategies based on low-work-function metals[19] or inorganic salts[20,21] can facilitate electron injection or extraction. However, their susceptibility to ambient degradation and frequent reliance on vacuum-based deposition processes impose inherent limitations on the device stability and scalable fabrication.[22] In contrast, conjugated polymer-based CILs offer distinct advantages including excellent solution processability, uniform film formation, and molecularly tunable energy levels. Among them, poly[(9,9-bis(3′-((*N*,*N*-dimethyl)-*N*-ethylammonium)-propyl)-2,7-fluorene)-alt-2,7-(9,9-dioctylfluorene)]dibromide (PFN-Br) has become the most widely adopted polymeric CIL for organic optoelectronic devices.[23–25] Nevertheless, the highest occupied molecular orbital (HOMO) levels of most available polymer CILs remain insufficiently deep to satisfy the stringent hole-blocking requirements of low-noise OPDs, resulting in the incomplete suppression of hole back-injection and persistently elevated dark current.[23,26,27] Accordingly, the de-

* Corresponding authors, E-mail: xxshao@ciac.ac.cn (X.X.S.)
E-mail: liujun@ciac.ac.cn (J.L.)
Invited Research Article
Received January 13, 2026; Accepted February 14, 2026; Published online May 14, 2026

velopment of polymeric CILs featuring deep-lying HOMO energy levels (E_{HOMO}) is both critically important and intrinsically challenging.[28] Beyond energetic alignment, CIL materials for OPD applications must also meet additional stringent criteria, including orthogonal solubility to preserve multilayer device integrity during solution processing, as well as an intrinsic ability to lower the cathode work function to establish an efficient Ohmic contact. These coupled requirements highlight the urgent need for new polymeric cathode interlayers that simultaneously deliver strong hole-blocking capability, processing compatibility, and stable cathode modification for high-performance OPDs.[28,29]

Recently, we developed a series of acceptor-acceptor (A-A) type B←N-based conjugated polymers that exhibit pronounced electron-deficient characteristics together with excellent n-type charge-transport properties.[30–33] Building on this molecular design concept, herein, we report an alcohol-soluble n-type polymeric CIL featuring a deep-lying E_{HOMO} for high-performance OPDs. The designed polymer, denoted as PBN27-OEG, incorporated B←N units along the conjugated main chain and was functionalized with polar oligo(ethylene glycol) (OEG) side chains (Scheme 1a). The introduction of B←N units enables PBN27-OEG to simultaneously achieve a deep E_{HOMO} of −5.88 eV and a low-lying lowest unoccupied molecular orbital (LUMO) energy level (E_{LUMO}) of −3.91 eV, which are highly favorable for effective hole blocking and electron transport at the cathode interface. In addition, the polar functional groups not only endow the polymer with excellent alcohol solubility for orthogonal processing but also induce effective cathode work-function modulation, thereby facilitating efficient electron extraction. As a result, OPDs incorporating PBN27-OEG as the CIL exhibit an ultralow dark current density of 1.66×10^{-9} A·cm^{-2} at −1 V, which is one order of magnitude lower than that of devices based on the benchmark CIL material PFN-Br, owing to the substantially enhanced hole-blocking capability. Benefiting from the suppressed dark current and efficient charge extraction, the resulting NIR OPDs deliver a high responsivity of 0.50 A·W^{-1} and a specific detectivity of up to 1.86×10^{12} Jones. To the best of our knowledge, this work represents the first demonstration of B←N conjugated polymers serving as CIL in organic optoelectronic devices, highlighting the potential of the B←N unit for interfacial engineering in high-performance OPDs.

EXPERIMENTAL

Molecular Design

As illustrated in Scheme 1(a), the polymer main chain was constructed by an alternating copolymer of double B←N bridged bipyridine (BNBP) and benzobisthiazole (BBTz) units. Both BNBP and BBTz function as strong electron-accepting moieties, resulting in an A-A type backbone that affords the polymer low-lying E_{LUMO} and E_{HOMO}.[30–32,34–36] A linear 2,5,8,11-tetraoxatridecane side chain is introduced into the BNBP unit. This polar OEG side chain endowed PBN27-OEG with good solubility in alcohol solvents, enabling orthogonal solution processing of the photoactive layer. Furthermore, the polar OEG side chain is expected to induce favorable interfacial dipoles at the electrode surface,

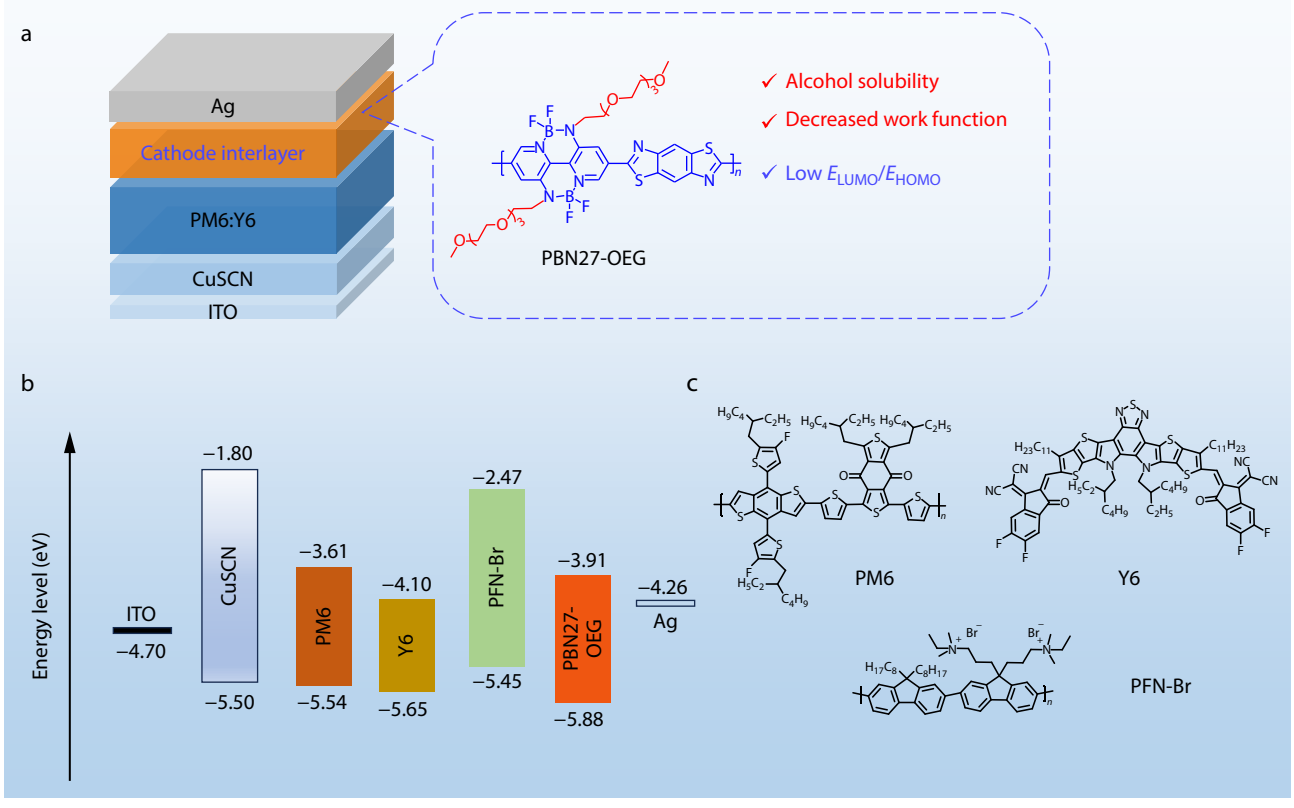

Scheme 1 (a) The OPD device architecture and the chemical structure of PBN27-OEG; (b) Energy level diagram of the OPD devices; (c) Chemical structures of the materials used in the OPDs.

thereby reducing the electrode work function and facilitating efficient electron extraction.

Materials

All solvents and reagents were purchased from commercial suppliers and used as received, unless otherwise stated. Anhydrous dichloromethane (CH_2Cl_2) was used as a solvent. Anhydrous toluene and tetrahydrofuran were dried over sodium and distilled before use. Compounds **1** and BBTz-Sn were synthesized according to previously reported procedures.[30–33]

Synthesis and Characterization

*Synthesis of compound **2***

A mixture of compound **1** (105.0 mg, 0.30 mmol) and NaH (61.0 mg, 1.50 mmol) was dissolved in anhydrous THF (2 mL) under an argon atmosphere and heated at 75 °C for 2.5 h. Then, 13-iodo-2,5,8,11-tetraoxatridecane (388.4 mg, 1.20 mmol) was added dropwise *via* syringe. The resulting mixture was then stirred at 75 °C for 5 h. After cooling to room temperature, the mixture was transferred to a round bottomed flask. The solvent was removed under reduced pressure, and the crude product was purified by silica gel column chromatography using petroleum ether/ethyl acetate/MeOH (2.00/1.00/0.15, *V*/*V*/*V*) as the eluent to give 2 as an orange oil (65.0 mg, 0.09 mmol, 30% yield). ^{1}H-NMR (500 MHz, $CDCl_3$, δ, ppm): 9.80 (s, 2H), 7.88 (s, 2H), 7.16 (s, 2H), 3.78 (t, *J*=5.4 Hz, 4H), 3.71–3.61 (m, 24H), 3.53 (dt, *J*=5.7, 2.6 Hz, 4H), 3.36 (s, 3H).

Synthesis of BNBP-OEG

Compound **2** (110 mg, 0.15 mmol) was dissolved in anhydrous CH_2Cl_2 (2 mL) under argon and heated to 70 °C. Then, $BF_3{\cdot}Et_2O$ (0.86 mL, 6.00 mmol) and Et_3N (1.52 mL, 12.00 mmol) were added dropwise *via* syringe. The resulting mixture was then stirred at 70 °C for 4 h. After cooling to room temperature, the mixture was extracted using CH_2Cl_2 and water. The organic layer was washed three times with brine and dried over Na_2SO_4. The solvent was evaporated under reduced pressure, and the residue was purified by column chromatography (silica gel, ethyl acetate) to give BNBP-OEG as an orange-red solid (76 mg, 0.12 mmol, 91% yield). ^{1}H-NMR (500 MHz, $CDCl_3$, δ, ppm): 8.18 (s, 2H), 8.17 (s, 2H), 3.80–3.77 (m, 8H), 3.65–3.61 (m, 20H), 3.55–3.53 (m, 4H), 3.37 (s, 3H). ^{13}C-NMR (126 MHz, $CDCl_3$, δ, ppm): 144.80, 128.74, 126.85, 124.76, 121.65, 71.79, 71.15, 70.82, 70.55, 70.52, 70.46, 70.35, 58.83, 44.05.

Synthesis of PBN27-OEG

A mixture of BNBP-OEG (54.0 mg, 0.07 mmol), BBTz-Tin (34.4 mg, 0.07 mmol), $Pd(PPh_3)_4$ (2.3 mg, 0.0021 mmol), and CuI (1.2 mg, 0.007 mmol) was dissolved in anhydrous toluene (2.5 mL) under an argon atmosphere. The mixture was then stirred at 120 °C for 0.5 h. After cooling to room temperature, the reaction mixture was poured into methanol. The crude polymer was purified by Soxhlet extraction using acetone, hexane, and hexafluoroisopropanol. The hexafluoroisopropanol fraction was then concentrated and poured into methanol. The resulting precipitate was collected and dried under vacuum to afford PBN27-OEG as a bright red solid (40.0 mg, 0.06 mmol, 93% yield). M_n=24.0 kDa, M_w=37.0 kDa, PDI= 1.5.

RESULTS AND DISCUSSION

Synthesis and Characterization of PBN27-OEG

Scheme 2 illustrates the synthetic route to the target polymer PBN27-OEG. The OEG side chains were synthesized according to a previously reported method. The key monomer, BNBP-OEG, was obtained by nucleophilic substitution of the BNBP precursor with an iodinated linear OEG chain. BBTz-Tin was synthesized according to literature procedures. Subsequently, PBN27-OEG was prepared *via* the Pd-catalyzed Stille polymerization of BNBP-OEG and BBTz-Tin. The resulting polymer was readily soluble in hexafluoroisopropanol (HFIP) at room temperature but insoluble in common chlorinated solvents, such as chloroform and chlorobenzene, thereby satisfying the requirement for orthogonal solvent processing. The molecular weight of the polymer was estimated *via* gel permeation chromatography (GPC) using HFIP as the eluent. PBN27-OEG exhibited a number-average molecular weight (M_n) of 24.0 kDa and polydispersity index (PDI) of 1.5 (Fig. S1 in the electronic supplementary information, ESI). Thermogravimetric analysis (TGA) confirmed the good thermal stability of PBN27-OEG, with a thermal decomposition temperature (T_d) of 318 °C at 5% weight loss (Fig. S2 in ESI).

Optoelectronic Properties

Fig. 1(a) presents the UV-Vis absorption spectra of PBN27-OEG in solution and in the thin-film state. The PBN27-OEG film exhibits a maximum absorption wavelength (λ_{max}) at 622 nm,

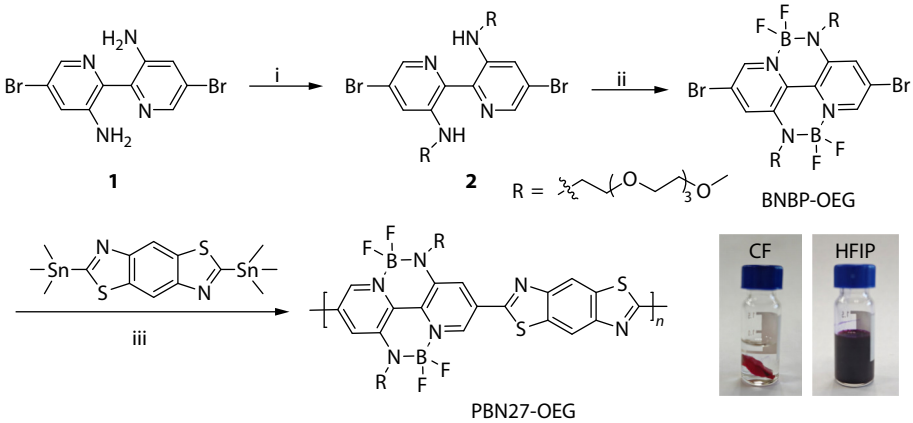

Scheme 2 Synthetic routes to PBN27-OEG. Reagents and conditions: (i) NaH, tetrahydrofuran (THF), 13-iodo-2,5,8,11-tetraoxatridecane, 80 °C; (ii) Et_3N, $BF_3.Et_2O$, 70 °C; (iii) $Pd(PPh_3)_4$, CuI, toluene, 120 °C. The pictures of PBN27-OEG in CF and HFIP.

which is red-shifted by 29 nm relative to its solution spectrum, indicating enhanced molecular aggregation and strengthened interchain interactions in the solid state. The cyclic voltammetry (CV) curve of the PBN27-OEG film spin-coated on a glassy carbon electrode is shown in Fig. 1(b). From the onset reduction and oxidation potentials, the E_{LUMO} and E_{HOMO} of PBN27-OEG were estimated to be –3.91 and –5.88 eV, respectively. The deep-lying E_{LUMO} and E_{HOMO} are attributed to the strong electron-accepting nature of the A-A type backbone, which is further supported by density functional theory (DFT) calculations on the model dimer. As shown in Fig. S8 (in ESI), molecular electrostatic potential (MEP) mapping reveals a pronounced positive potential region localized around the B←N coordination bond, confirming its strong electron-withdrawing character. This feature directly contributes to the lowered HOMO level and creates electrophilic positions that can facilitate intermolecular electron transport, correlating well with the higher electrical conductivity observed in the PBN27-OEG thin films.

To gain deeper insight into the electronic structure, we systematically characterized the thin films of PBN27-OEG and the reference material PFN-Br using ultraviolet photoelectron spectroscopy (UPS) (Fig. 1c). The secondary electron cutoff and valence band regions were used to determine the E_{HOMO} of PBN27-OEG and PFN-Br to be –5.97 and –5.45 eV, respectively, with the corresponding E_{LUMO} calculated as –4.09 and –2.47 eV. Benefiting from the synergistic effect of the A-A backbone and B←N bond, PBN27-OEG possesses a deeper E_{HOMO}, which is 0.52 eV lower than that of PFN-Br, promising its superior hole-blocking capability. Furthermore, the E_{LUMO} of PBN27-OEG aligns well with that of the common electron acceptors in the OPD active layer, facilitating efficient electron transport. In contrast, the excessively high E_{LUMO} of PFN-Br is expected to create an energy barrier for electron transport at the interface.

The UPS measurements further elucidated the work function (W_F) modification capability of these materials. After spin-coating thin layers of PBN27-OEG and PFN-Br onto a silver electrode, the W_F significantly decreased from 4.26 eV to 3.70 and 3.50 eV, corresponding to substantial reductions of 0.56 and 0.76 eV, respectively. This phenomenon is primarily ascribed to the interfacial dipole layer induced by the polar OEG side chains of the polymers. The reduction in W_F is crucial for forming an Ohmic contact at the cathode,[37] thereby enabling barrier-free electron extraction. Moreover, conductivity measurements *via* the two-probe method revealed that PBN27-OEG possesses a high electrical conductivity of 1.36×10^{-6} S·cm^{-1}, which is nearly two orders of magnitude greater than that of PFN-Br (2.58×10^{-8} S·cm^{-1}). In summary, PBN27-OEG integrates a deep E_{HOMO}, a well-aligned E_{LUMO}, effective W_F modification capability, and high conductivity. These multifaceted advantages provide a solid foundation for their application as a high-performance cathode interlayer.

OPD devices with PBN27-OEG or PFN-Br as the cathode interlayer (CIL), as well as devices without a CIL, were fabricated using a conventional architecture of ITO/CuSCN/PM6:Y6/CIL/Ag. The chemical structures of the photoactive materials (PM6 and Y6) and the reference CIL (PFN-Br) are shown in Scheme 1(b). A commercial p-type semiconductor, CuSCN, was used as the anode interlayer. To fabricate the multilayer device *via* solution processing, the CuSCN layer was thermally annealed at 150 °C for 15 min. The PM6:Y6 active layer was subsequently spin-coated with chloroform solution. The CILs were then deposited with orthogonal solvents: PFN-Br with the methanol solution and PBN27-OEG with the HFIP solution, ensuring the structural integrity of the underlying layers.

Fig. 2(a) presents the semi-logarithmic current density-voltage (*J-V*) characteristics of the three OPDs measured in the dark. At a reverse bias of –1 V, the control device without a CIL and the device incorporating PFN-Br as the CIL exhibited dark current densities (J_d) of 2.46×10^{-7} and 3.88×10^{-8} A·cm^{-2}, respectively. In stark contrast, the dark current density was significantly suppressed to 1.66×10^{-9} A·cm^{-2} for devices incorporating PBN27-OEG as the CIL. Remarkably, the J_d of the PBN27-OEG-based device is one order of magnitude lower than that of the PFN-Br-based device and two orders of magnitude lower than that of the CIL-free control. This superior performance is primarily attributed to the deep-lying E_{HOMO} of PBN27-OEG, which creates a higher energy barrier for charge recombination and hole injection, thereby effectively minimizing the dark current.

The spectral responsivities (R) of the devices at a bias voltage of –1 V are shown in Fig. 2(b). OPDs with both CILs demonstrated a high responsivity of approximately 0.5 A·W^{-1} across the detection range. Notably, the device with PBN27-OEG showed a marginally higher R than that of the CIL-free device, which can be ascribed to its more effective capability to lower the cathode work function, thereby facilitating superior electron extraction from the photoactive layer. The specific detectivity (D^*), a key figure of merit for OPDs, was calculated from the measured noise spectral density (S_n) at –1 V

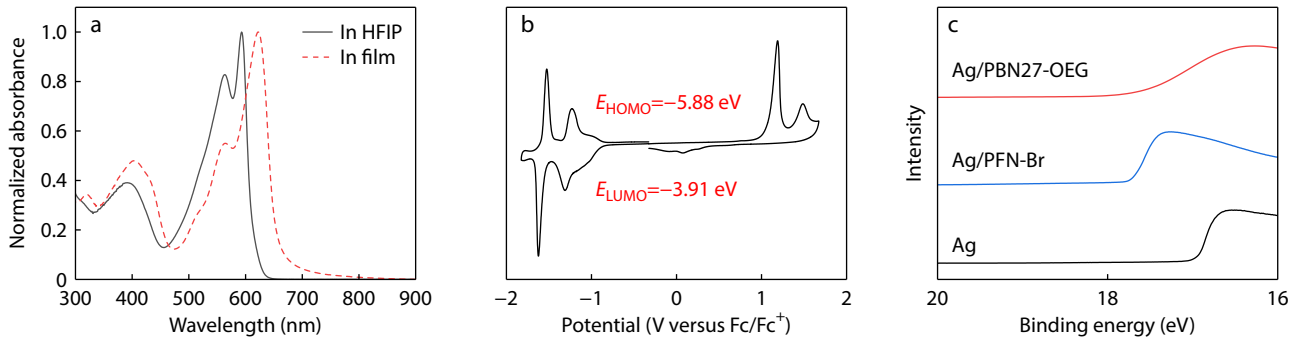

Fig. 1 (a) Normalized UV-Vis absorption spectra of PBN27-OEG in thin film and in solution; (b) Cyclic voltammograms of PBN27-OEG in thin film; (c) UPS spectra of the CILs and the secondary electron cut-off region of the UPS spectra for CILs spin-coated on Ag electrodes.

https://doi.org/10.1007/s10118-026-3628-3

bias, as shown in Fig. 2(c). The PBN27-OEG based device yielded the lowest noise current density of 7.62×10^{-14} A·Hz$^{-1/2}$ at 1 kHz, which is one order of magnitude lower than that of the other two devices. This exceptionally low noise floor, consistent with its ultralow dark current, underscores the outstanding noise-suppression capability of the PBN27-OEG interlayer. D^* can be accurately determined from the noise current density shown in Fig. 2(d) using the following relationship:[38,39]

$$D^* = \frac{R\sqrt{AB}}{I_n} = \frac{R\sqrt{A}}{S_n} \quad (1)$$

where A is the device area, B is the detection bandwidth (Hz), and S_n is the noise spectral density measured at –1 V bias, encompassing all noise components, including shot, thermal, and 1/f noise. At 1 kHz, the maximum D^* values for the OPDs with PBN27-OEG, PFN-Br, and the control device without CIL reach 1.86×10^{12}, 3.60×10^{11}, and 1.80×10^{11} Jones, respectively. Remarkably, the device with PBN27-OEG surpasses the other two devices by approximately one order of magnitude in terms of detectivity, demonstrating its exceptional detection capability.

As shown in Fig. 3(a), the linear dynamic range (LDR) was characterized using a 625 nm laser source to evaluate the response of the detector to varying light intensities. The LDR is defined as the ratio between the maximum and minimum incident light power over which the photodetector maintains a linear relationship between its output photocurrent and input light intensity. LDR is calculated using the following formula:[40]

$$\mathrm{LDR} = 20\lg\left(\frac{I_{max}}{I_{min}}\right) \quad (2)$$

where I_{max} and I_{min} are the maximum and minimum detectable photocurrent, respectively. The PBN27-OEG-based device, with PBN27-OEG, achieves a superior LDR of 138 dB, significantly

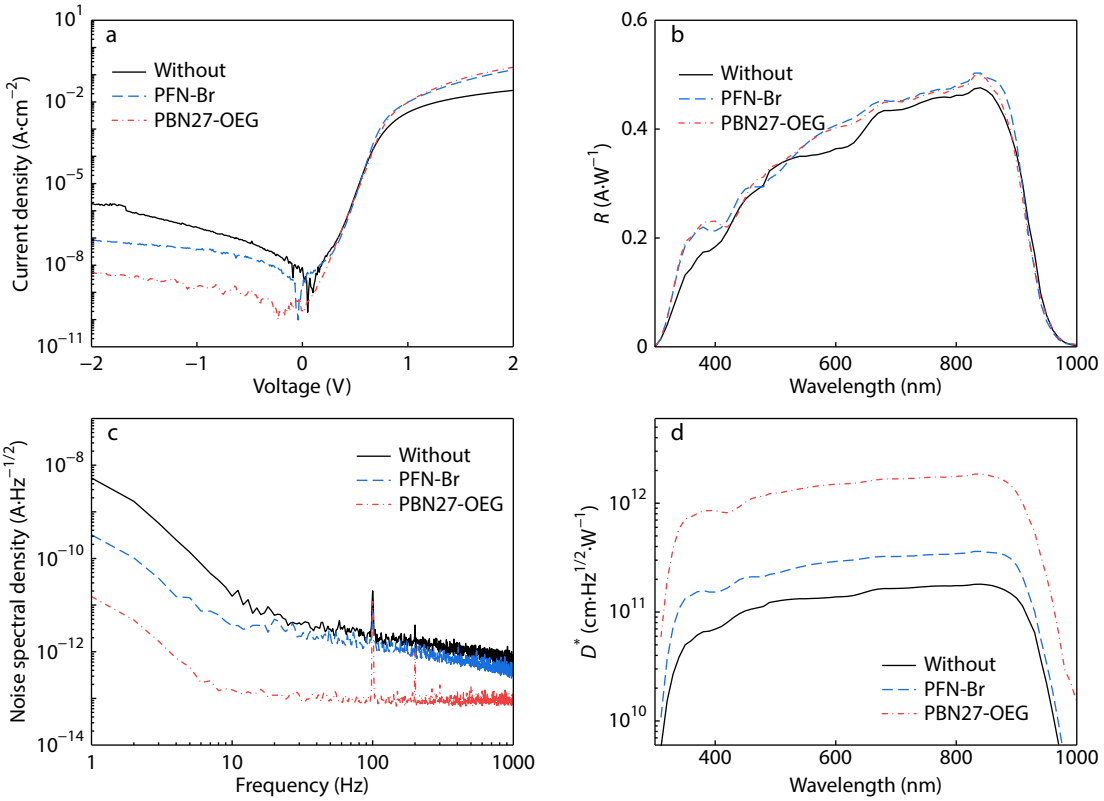

Fig. 2 (a) J_d-V characteristics, (b) responsivity, (c) noise spectral density, (d) specific detectivity at –1 V bias of the OPD devices with various CILs.

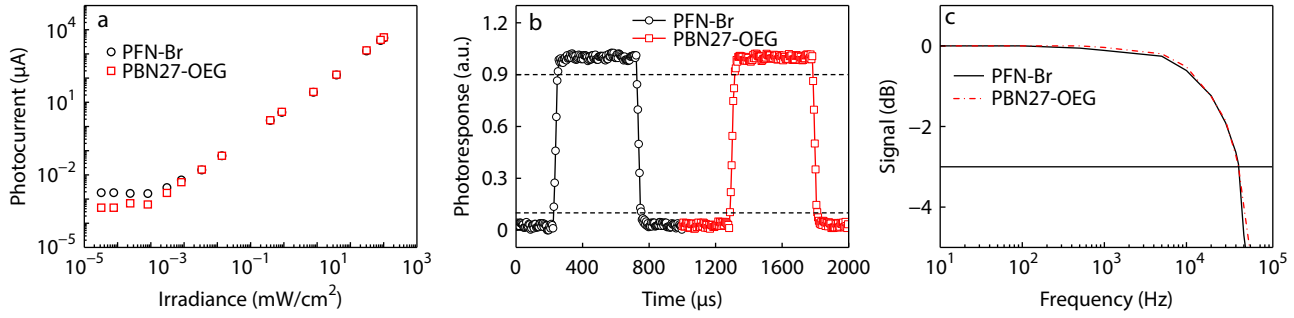

Fig. 3 (a) Linear dynamic range at –1 V bias; (b) Phototransient response, and (c) normalized response as a function of frequency of the OPD devices with various CILs.

https://doi.org/10.1007/s10118-026-3628-3

outperforming the PFN-Br-based device (124 dB). This result demonstrates that the PBN27-OEG-based device maintains a highly linear photoresponse over a considerably wider range of incident light intensities.

The response speed of OPDs to optical signals is critical for their applications in information communication and image processing. It is evaluated by the rise (from 10% to 90% of the steady-state value) and fall (from 90% to 10%) times of the photocurrent. As shown in Fig. 3(b), at a modulation frequency of 1 kHz, the PBN27-OEG-based device exhibits rise and fall times of 29 and 27 μs, respectively, which are comparable to those of the PFN-Br-based device. The –3 dB cutoff frequency (f_{-3dB}) is another key parameter for assessing the operational bandwidth of photodetectors. All devices with different CILs show similar f_{-3dB} values of approximately 43 kHz, as depicted in Fig. 3(c).

The stability of the interfacial layer in the device is a critical metric for evaluating its practical application potential. In this study, we evaluated the thermal stability of OPDs based on PBN27-OEG and PFN-Br. The normalized performance retention (initial D_{sh}^{*}=100%) of the unencapsulated devices was monitored during thermal aging at 100 °C under a nitrogen atmosphere. As shown in Fig. S10 (in ESI), the device incorporating PBN27-OEG exhibited excellent stability, retaining approximately 75% of its initial performance after 12 h of continuous heating. In contrast, the PFN-Br-based device degraded rapidly at the initial stage, with its performance decreasing to 50% of the initial value within 0.5 h. These results indicate that PBN27-OEG possesses good thermal stability and is promising for practical applications.

Mechanism Analysis

To elucidate the origin of the low J_d and high D^* in PBN27-OEG-based devices, we employed electrochemical impedance spectroscopy (EIS) in the dark to estimate the shunt resistance (R_{sh}) of the OPDs. As derived from the EIS results (Fig. 4a), the PBN27-OEG-based device exhibits a substantially larger R_{sh} of 350 kΩ compared to 200 kΩ for the PFN-Br-based device. This higher R_{sh} indicates the superior capability of the PBN27-OEG interlayer to block hole injection, which is consistent with the larger energy barrier for holes at the interface, as evidenced by the deeper E_{HOMO} of PBN27-OEG. Furthermore, electron-only devices (ITO/ZnO/PM6:Y6/CIL/Ag) were fabricated to evaluate electron transport properties using the space-charge-limited current (SCLC) method. The *J-V* characteristics of the devices are shown in Fig. S5 (in ESI), respectively. The electron mobility was estimated to be 1.24×10^{-3} $cm^2\cdot V^{-1}\cdot s^{-1}$ for the PBN27-OEG-based device and 1.77×10^{-3} $cm^2\cdot V^{-1}\cdot s^{-1}$ for the PFN-Br-based device. The comparable electron mobility values suggest unhindered electron extraction and transport in both the devices. Therefore, the PBN27-OEG CIL not only effectively blocks hole injection but also facilitates efficient electron extraction and transport, collectively contributing to the superior OPD performance. To elucidate the charge extraction capability of PBN27-OEG, we further investigated its interfacial charge transfer behavior using photoluminescence (PL) spectroscopy. The PL spectra of the pristine Y6 film and the Y6/PBN27-OEG blend film were measured under 808 nm excitation, which selectively excites the Y6 component (Fig. S12 in ESI). The results show that the Y6/PBN27-OEG blend film exhibits significant PL quenching compared to the pristine Y6 film, with a calculated quenching efficiency as high as 77.4%. This result directly confirms the occurrence of efficient photoinduced charge transfer—specifically, electron injection from Y6 to PBN27-OEG—at the Y6/PBN27-OEG interface, providing key photophysical evidence for its outstanding electron extraction capability.

The dark current in OPDs primarily comprises two components: thermal generation current and injection current. The thermal generation current has been shown to correlate with the charge-transfer state energy (ΔE_{CT}), defined as the energy

Table 1 Performance of OPD devices with various CILs at –1 V bias.

Sample	J_d (A·cm^{-2})	R (A·W^{-1})	$S_{n,1kHz}$ (A·Hz$^{-1/2}$)	D^* (cm·Hz$^{1/2}$·W^{-1})	D_{sh}^* (cm·Hz$^{1/2}$·W^{-1})
Without CIL	2.46×10^{-7}	0.476	7.47×10^{-13}	1.80×10^{11}	1.69×10^{12}
PFN-Br	3.88×10^{-8}	0.503	3.95×10^{-13}	3.60×10^{11}	4.53×10^{12}
PBN27-OEG	1.66×10^{-9}	0.500	7.62×10^{-14}	1.86×10^{12}	2.16×10^{13}

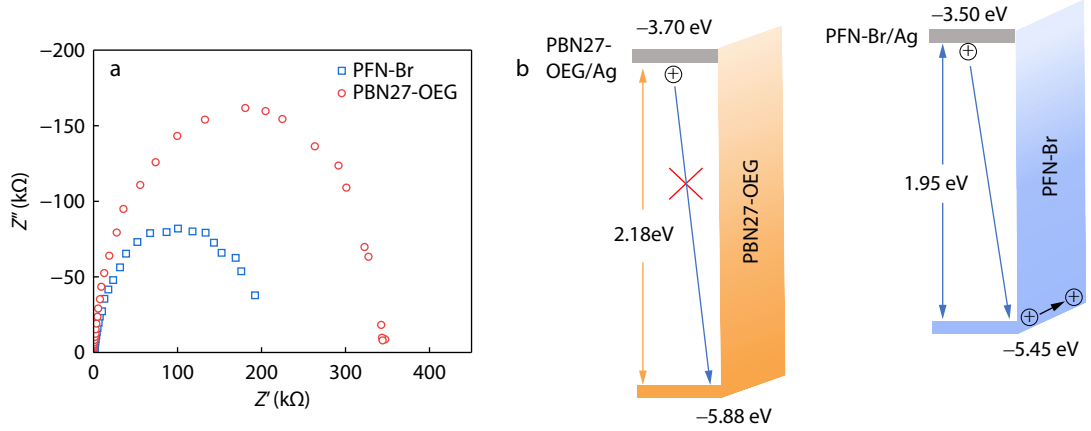

Fig. 4 (a) Nyquist plots of the OPD devices with different cathode interlayers under dark conditions; (b) The schematic diagram of the hole injection barrier.

difference between the HOMO of the donor and the LUMO of the acceptor. For devices employing the same photoactive layer, the contribution from the thermal generation current is comparable and thus negligible in this comparative study. Consequently, the variation in J_d among the OPDs with different CILs is predominantly governed by the injection current, which is critically determined by the hole injection barrier at the cathode interface. A schematic energy level diagram (Fig. 4b) illustrates the relationship between the hole injection barrier and the energy levels of the CIL. The hole injection barrier heights for OPDs with PBN27-OEG and PFN-Br as CILs are calculated to be 2.18 and 1.95 eV, respectively. The larger hole injection barrier in the PBN27-OEG-based device effectively suppresses hole injection from the electrode under reverse bias, serving as the primary factor for its significantly reduced dark current.

Beyond the energy level advantage, the exceptionally low dark current is further ensured by the superior interfacial properties of PBN27-OEG. Atomic force microscopy (AFM) reveals that the PBN27-OEG film forms a smoother and more continuous surface (RMS=2.42 nm) than its PFN-Br counterpart (RMS=2.80 nm), effectively blocking direct leakage pathways. AFM height images of the PM6:Y6 blend film and the PBN27-OEG or PFN-Br films deposited on top of the PM6:Y6 blend film are shown in Fig. S6 (in ESI). In addition, as shown in Fig. S9 (in ESI), the trap-state density (N_t) was determined from the *J-V* characteristics of the single-carrier device, which is significantly lower for PBN27-OEG (5.3×10^{14} cm^{-3}) compared to PFN-Br (1.2×10^{15} cm^{-3}). This reduced trap density helps suppress trap-assisted charge recombination and tunneling. Therefore, in addition to the dominant contribution from the optimal energy-level alignment, a smoother film morphology and reduced trap density also contribute to the suppressed dark current.

CONCLUSIONS

In summary, we successfully designed and synthesized a novel alcohol-soluble n-type conjugated polymer that innovatively integrates a B←N unit with OEG-based side chains. This polymer exhibits a deep-lying E_{HOMO} (–5.88 eV), appreciable electrical conductivity (1.36×10^{-6} $S\cdot cm^{-1}$), and the ability to effectively lower the cathode work function by approximately 0.55 eV, thereby enabling excellent Ohmic contact with the active layer. When employed as a cathode interlayer in OPDs, the high hole-injection barrier resulting from its deep-lying E_{HOMO} contributes to remarkable suppression of dark current (1.66×10^{-9} $A\cdot cm^{-2}$) and outstanding D^* of 1.86×10^{12} Jones. This work demonstrates, for the first time, the feasibility of B←N-based polymers as high-performance cathode interlayers for OPDs and also establishes a new molecular design paradigm for developing next-generation interfacial materials with precisely tailored energy levels.

Conflict of Interests

Li-Xiang Wang is an associate editor for *Chinese Journal of Polymer Science* and was not involved in the editorial review or the decision to publish this article. All authors declare that there are no competing interests.

Electronic Supplementary Information

Electronic supplementary information (ESI) is available free of charge in the online version of this article at http://doi.org/10.1007/s10118-026-3628-3.

Data Availability Statement

The data that support the findings of this study are available from the corresponding author upon reasonable request.

ACKNOWLEDGMENTS

This work was financially supported by the Strategic Priority Research Program of the Chinese Academy of Sciences (No. XDB0520103), the CAS Project for Young Scientists in Basic Research (No. YSBR-110), the National Natural Science Foundation of China (Nos. 22135007, 22305245 and 22361132545) and the Jilin Province and Chinese Academy of Sciences Cooperative High-Tech Industrialization Special Fund Project (No. 2025SYHZ0019).

REFERENCES

1 Xia, Y.; Zhang, J.; Guo, T.; Wang, H.; Geng, C.; Zhu, Y.; Han, R.; Yang, Y.; Song, G.; Wan, X.; Li, G.; Chen, Y. High-speed flexible near-infrared organic photodetectors for self-powered optical integrated sensing and communications. *Adv. Funct. Mater.* **2025**, *35*, 2412813.
2 Li, T.; Hu, G.; Wu, H.; Ding, L.; Zhang, J.; Sun, M.; Li, Y.; Liu, Z.; Shao, Y.; Fang, Y.; Qiao, Y.; Shen, L.; Lin, Y. Highly sensitive water pollution monitoring using colloid-processed organic photodetectors. *Nat. Water.* **2024**, *2*, 577–588.
3 Jansen-van Vuuren, R. D.; Armin, A.; Pandey, A. K.; Burn, P. L.; Meredith, P. Organic photodiodes: The future of full color detection and image sensing. *Adv. Mater.* **2016**, *28*, 4766–4802.
4 Yokota, T.; Nakamura, T.; Kato, H.; Mochizuki, M.; Tada, M.; Uchida, M.; Lee, S.; Koizumi, M.; Yukita, W.; Takimoto, A.; Someya, T. A conformable imager for biometric authentication and vital sign measurement. *Nat. Electron.* **2020**, *3*, 113–121.
5 Sandberg, O. J.; Kaiser, C.; Zeiske, S.; Zarrabi, N.; Gielen, S.; Maes, W.; Vandewal, K.; Meredith, P.; Armin, A. Mid-gap trap state-mediated dark current in organic photodiodes. *Nat. Photon.* **2023**, *17*, 368–374.
6 Huang, Y. C.; Wang, T. Y.; Huang, Z. H.; Santiago, S. R. M. S. Advancing detectivity and stability of near-infrared organic photodetectors *via* a facile and efficient cathode interlayer. *ACS Appl. Mater. Interfaces* **2024**, *16*, 27576–27586.
7 Zhong, Z. M.; Peng, F.; Ying, L.; Huang, Z. Q.; Zhong, W. K.; Yu, G.; Cao, Y.; Huang, F. Infrared photodetectors and image arrays made with organic semiconductors. *Chinese J. Polym. Sci.* **2023**, *41*, 1629–1637.
8 Zhou, Y.; Li, M.; Guo, Y.; Lu, H.; Song, J.; Bo, Z.; Wang, H. Dibenzopyran-based wide band gap conjugated copolymers: Structural design and application for polymer solar cells. *ACS Appl. Mater. Interfaces* **2016**, *8*, 31348–31358.
9 Chow, P. C. Y.; Someya, T. Organic photodetectors for next-generation wearable electronics. *Adv. Mater.* **2020**, *32*, 1902045.
10 Yang, D.; Ma, D. Development of organic semiconductor photodetectors: From mechanism to applications. *Adv. Opt. Mater.* **2019**, *7*, 1800522.
11 Wang, C.; Zhang, X.; Hu, W. Organic photodiodes and

Graphical Abstract

A Polymer Cathode Interlayer Based on B←N Unit for Suppressed Dark Current in Organic Photodetectors

Yu-Xin Xi, Ke Jia, Jia-Hui Wang, Xu Cao, Si-Hui Deng, Jun-Hui Miao, Xing-Xin Shao, Jun Liu, and Li-Xiang Wang

University of Science and Technology of China; Changchun Institute of Applied Chemistry, Chinese Academy of Sciences

A B←N-based alcohol-soluble n-type polymer cathode interlayer (CIL) with deep HOMO energy level (−5.88 eV) enables enlarged hole-blocking barrier, achieving ultralow dark current (1.66×10^{-9} A·cm^{-2}) and high detectivity (1.86×10^{12} Jones) in near-infrared organic photodetectors.

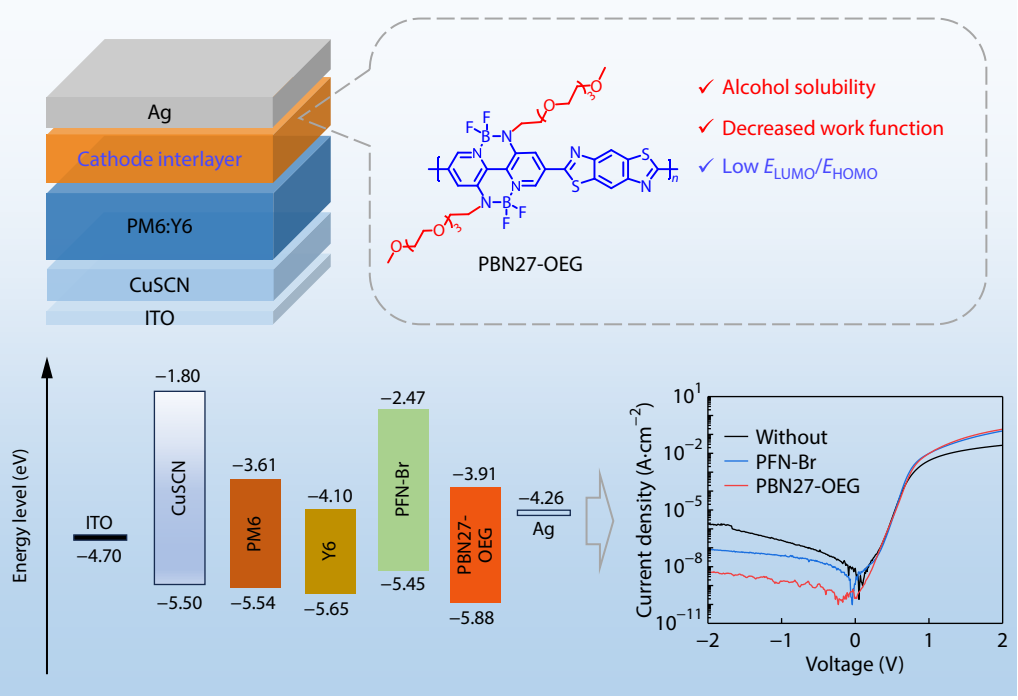

Chinese J. Polym. Sci. 2026, 44, 2144–2152 *https://doi.org/10.1007/s10118-026-3628-3*

phototransistors toward infrared detection: materials, devices, and applications. *Chem. Soc. Rev.* **2020**, *49*, 653–670.

12 Xu, G.; Hu, X.; Liao, X.; Chen, Y. Bending-stability interfacial layer as dual electron transport layer for flexible organic photovoltaics. *Chinese J. Polym. Sci.* **2021**, *39*, 1441–1447.

13 Chen, W.; Zhang, Y.; Zhu, X.; Miao, J.; Liu, J.; Wang, L. Near-infrared organic photodetectors outperform Si photodetectors: Introducing an all-fused-ring acceptor into active layers for ultra-low trap density. *Sci. China Mater.* **2025**, *68*, 1359–1368.

14 Qiu, H.; Zhong, Z.-m.; Li, M.-j.; Ying, L.; Yu, G.; Huang, F.; Cao, Y. Achieving high-detectivity near infrared organic photodetectors through optimizing film thickness and polymer molecular weight. *Acta Polymerica Sinica* (in Chinese) **2022**, *53*, 433–440.

15 Yang, Y.; Wang, J.; Zu, Y.; Liao, Q.; Zhang, S.; Zheng, Z.; Xu, B.; Hou, J. Robust and hydrophobic interlayer material for efficient and highly stable organic solar cells. *Joule* **2023**, *7*, 545–557.

16 You, Z.; Song, Y.; Liu, W.; Wang, W.; Zhu, C.; Duan, Y.; Liu, Y. Diazabicyclic electroactive ionenes for efficient and stable organic solar cells. *Angew. Chem. Int. Ed.* **2023**, *62*, e202302538.

17 Yip, H.-L.; Jen, A. K. Y. Recent advances in solution-processed interfacial materials for efficient and stable polymer solar cells. *Energy Environ. Sci.* **2012**, *5*, 5994–6011.

18 Hu, J. Q.; Jiang, J. L.; Dai, S. X.; Liu, H.; Cui, L. X.; Song, H. X.; Jiang, H. Q.; Huang, M. H. Benzodithiophene-functionalized naphthalimide cathode interlayers for organic solar cell. *Acta Polymerica Sinica* (in Chinese) **2025**, *56*, 1140–1149.

19 Li, G.; Shrotriya, V.; Huang, J.; Yao, Y.; Moriarty, T.; Emery, K.; Yang, Y. High-efficiency solution processable polymer photovoltaic cells by self-organization of polymer blends. *Nat. Mater.* **2005**, *4*, 864–868.

20 Ueno, K.; Matsubara, K.; Watanabe, M.; Takeoka, Y. An electro- and thermochromic hydrogel as a full-color indicator. *Adv. Mater.* **2007**, *19*, 2807–2812.

21 Huang, J.; Li, G.; Wu, E.; Xu, Q.; Yang, Y. Achieving high-efficiency polymer white-light-emitting devices. *Adv. Mater.* **2006**, *18*, 114–117.

22 Yi, C.; Hu, X.; Gong, X.; Elzatahry, A. Interfacial engineering for high performance organic photovoltaics. *Mater. Today* **2016**, *19*, 169–177.
23 Huang, F.; Wu, H.; Wang, D.; Yang, W.; Cao, Y. Novel electroluminescent conjugated polyelectrolytes based on polyfluorene. *Chem. Mater.* **2004**, *16*, 708–716.
24 Zheng, Y.; Zhao, J.; Liang, H.; Zhao, Z.; Kan, Z. Double-dipole induced by incorporating nitrogen-bromine hybrid cathode interlayers leads to suppressed current leakage and enhanced charge extraction in non-fullerene organic solar cells. *Adv. Sci.* **2023**, *10*, 2302460.
25 Xu, C.; Liu, P.; Feng, C.; He, Z.; Cao, Y. Organic photodetectors with high detectivity for broadband detection covering uv-vis-nir. *J. Mater. Chem. C* **2022**, *10*, 5787–5796.
26 Yao, J.; Qiu, B.; Zhang, Z. G.; Xue, L.; Wang, R.; Zhang, C.; Chen, S.; Zhou, Q.; Sun, C.; Yang, C.; Xiao, M.; Meng, L.; Li, Y. Cathode engineering with perylene-diimide interlayer enabling over 17% efficiency single-junction organic solar cells. *Nat. Commun.* **2020**, *11*, 2726.
27 Jia, T.; Zhou, W.; Li, F.; Gao, Y.; Wang, L.; Han, J.; Zhang, J.; Wang, Y. Alcohol/water-soluble porphyrins as cathode interlayers in high-performance polymer solar cells. *Sci. China Chem* **2015**, *58*, 323–330.
28 Yu, Y.; Wang, J.; Chen, Z.; Xiao, Y.; Fu, Z.; Zhang, T.; Yuan, H.; Hao, X.-T.; Ye, L.; Cui, Y.; Hou, J. Naphthalene diimide-based cathode interlayer material enables 20.2% efficiency in organic photovoltaic cells. *Sci. China Chem* **2024**, *67*, 4194–4201.
29 Yang, Y.; Wang, J.; Xiao, Y.; Xu, B.; Hou, J. Understanding the interfacial energy structure and electron extraction process in inverted organic solar cells with phosphine-doped cathode interlayers. *Chin. J. Chem* **2024**, *42*, 1347–1354.
30 Long, X.; Ding, Z.; Dou, C.; Zhang, J.; Liu, J.; Wang, L. Polymer acceptor based on double B←N bridged bipyridine (bnbp) unit for high-efficiency all-polymer solar cells. *Adv. Mater.* **2016**, *28*, 6504–6508.
31 Long, X.; Dou, C.; Liu, J.; Wang, L. Fine-tuning lumo energy levels of conjugated polymers containing a B←N unit. *Macromolecules* **2017**, *50*, 8521–8528.
32 Zhao, R.; Wang, N.; Yu, Y.; Liu, J. Organoboron polymer for 10% efficiency all-polymer solar cells. *Chem. Mater.* **2020**, *32*, 1308–1314.
33 Cao, X.; Li, H.; Hu, J.; Tian, H.; Han, Y.; Meng, B.; Liu, J.; Wang, L. An amorphous n-type conjugated polymer with an ultra-rigid planar backbone. *Angew. Chem. Int. Ed.* **2023**, *62*, e202212979.
34 Ahmed, E.; Kim, F. S.; Xin, H.; Jenekhe, S. A. Benzobisthiazole–thiophene copolymer semiconductors: synthesis, enhanced stability, field-effect transistors, and efficient solar cells. *Macromolecules* **2009**, *42*, 8615–8618.
35 Liu, B. Y.; Xie, C.; Ge, C. W.; Cui, M. M.; Yang, W.; Ma, Z. F.; Gao, X. K.; Zhou, Y. H.; Zhang, Q. Benzobisthiazole polymer with resonance-assisted hydrogen bonds for high-performance transistor and solar cell applications. *Chinese J. Polym. Sci.* **2022**, *40*, 147–156.
36 Ma, M.; Zhang, L.; Yao, T.; Yang, H.; Liu, J.; Liu, J. Extrinsic n-doping of a double B←N bridged bipyridine-based polymer containing oligoethylene glycol side chains. *Polym. Sci. Technol.* **2025**, *1*, 359–365.
37 Li, Y.; Li, T.; Wang, J.; Zhan, X.; Lin, Y. Intrinsically inert hyperbranched interlayer for enhanced stability of organic solar cells. *Sci. Bull.* **2022**, *67*, 171–177.
38 Song, Y.; Zhong, Z.; He, P.; Yu, G.; Xue, Q.; Lan, L.; Huang, F. Doping compensation enables high-detectivity infrared organic photodiodes for image sensing. *Adv. Mater.* **2022**, *34*, 2201827.
39 Liu, T.; Lin, Q.; Ma, Y.; Wang, S.; Chen, H.; Wei, Y.; Song, Y.; Shen, L.; Huang, F.; Huang, H. Multifunctional organic vertical photodiodes for photo-detection and photo-synapse enabled by modulation of the interface energy barrier. *Adv. Opt. Mater.* **2022**, *10*, 2201104.
40 Liu, T.; Jia, Z.; Song, Y.; Yu, N.; Lin, Q.; Li, C.; Jia, Y.; Chen, H.; Wang, S.; Wei, Y.; Lin, Y.; Huang, F.; Tang, Z.; Li, Y.; Meng, L.; Huang, H. Near infrared self-powered organic photodetectors with a record responsivity enabled by low trap density. *Adv. Funct. Mater.* **2023**, *33*, 2301167.